SAJSET
ISSN: 2992-3581

Savannah Journal of Science and Engineering Technology
Volume: 02; Issue: 05; Pages: 266-276; 2024.
www.sajsetjournal.com.ng

DOI: xx.xxxx.x/sajset-02-2024-0035

SAJSET
ISSN: 2992-3581

Wideband RCS reduction and gain enhancementh of MIMO antenna using polarization conversion metamaterial

[1]Abana, M. A., [2,3]Jabire, A. H. and [4]Dahiru, I.

[1]*Department of Electrical and Electronics Engineering, Modibbo Adama University, Yola, Adamawa State, Nigeria*
[2] *Department of Electrical and Communication Engineering, United Arab Emirates University, AL-Ain, United Arab Emirate*
[3] *Department of Electrical and Electronics Engineering, Taraba State University, Jalingo, Taraba State, Nigeria*
[4] *Air force Institute Technology Kaduna, Kaduna State, Nigeria*

Paper History

Received: 20th August, 2024
Accepted: 07th Sept., 2024
Published: September, 2024

Corresponding author
Abana, M. A.
m.a.abana@mau.edu.ng

Abstract:

A wideband MIMO antenna is presented in this paper that reduces monostatic radar cross-section (RCS). The reduction in RCS is achieved by substituting the reference antenna's ground plane with a ground plane of metamaterial unit cells designed for polarization conversion. The reference antenna is constructed using a Rogers R03003 substrate with dimensions of 1.5mm thickness and 0.009 loss tangent. Based on the proposed design, the MIMO antenna can operate at a wide impedance width of 2.8 – 6GHz. The system performance was validated through practical measurements. The antenna peak gain is 5.6dBi with 89% efficiency. Furthermore, the analysis of diversity conducted on the proposed MIMO antenna reveals that the antenna has a low correlation coefficient of 0f <0.001, channel capacity loss of less than 0.35bits/sec/Hz, and total active reflection coefficient of <-10Db. The measured isolation of <-22dB is realized with a maximum RCS reduction of 48 dB. The proposed MIMO antenna's radiation performance has been experimentally verified. The proposed MIMO antenna can be applied in the 6th generation radio access network as well as stealth technology.

Keywords: *Polarization, Metamaterial, Radar, MIMO, Circuit, wideband*

1. Introduction

The radar cross section (RCS) application is primarily found in military stealth technology because most military aircraft want to penetrate the enemy area without detection [1]. Deploying antennas in military applications led to a notable increase in radar cross-section. Consequently, researchers are keenly interested in reducing RCS for antennas.

So far, there have been many antenna RCS reduction technologies, such as phase gradient metasurface (PGM) [2], artificial magnetic conductors (AMC), and radar-absorbing materials (RAMs) [3]. The use of frequency selective surface (FSS) [4] and hybrid RAMs [5]. The RAM degrades the antenna performance. The use of metamaterials in reducing antenna RCS and electromagnetic interaction between N elements demonstrates the capability of artificial structures to manipulate electromagnetic waves to obtain unusual properties [6]. The metamaterial can reduce RCS by exploiting the cancellation effects caused by the 180^0 reflection phase difference [6].

Multiple-input-multiple-output (MIMO) methods, used in wireless communication to address the need for increased data throughput, are a promising solution. The challenge of enhancing isolation between the antenna elements while keeping the design compact has garnered significant research interest in recent years. Among various isolation techniques mentioned in studies of Thummaluru, *et al.* [7], Lu, *et al.* [8], Das, *et al.* [9] and Saxena, *et al.* [10], particular attention has been given to the defected ground structure (DGS) because it effectively reduces the electromagnetic interaction between antenna elements without requiring any additional structures [11].

The RCS of Das and Mandal [12] was reduced to a maximum of 7 dB using a cluster polarization converter. The studies of Gao, *et al.* [13] used a non-uniform metasurface to reduce the RCS of a circularly polarized antenna. The lowest RCS value remains above 6dB throughout the operational frequency range. In Soliman, *et al.* [14], a low-RCS antenna that relied on a metasurface featuring a polarization-dependent artificial magnetic conductor (AMC) was introduced. The RCS reduction of -15dB is realized throughout the operating frequency. The broadband low scattering characteristics are achieved by another adjacent antenna [15]. The low RCS was attained without using any additional structure. A coding metasurface concept was employed in Li *et al.* [16] to reduce the RCS of a microstrip patch antenna. A maximum reduction of 20dB is realized at 18GHz. In Zhang *et al.* [17], the study presents an integrated 2-bit coding metasurface-based array antenna that can reduce the RCS, covering an ample incidence angle space. As in Deng *et al.* [18], a 5dB RCS reduction from 3.7 – 6.7GHz is achieved based on polarization conversion metasurface, which features excellent potential for applications in low RCS platforms. An antenna under study is reduced in monostatic RCS using an Electromagnetic

Band Gap (EBG) structure [19]. The antenna's gain is enhanced due to the EBG properties, which effectively suppress the surface wave in the slot array. A polarization conversion metasurface antenna and gain improvement at the Ku band is reported in Deepti *et al.* [20]. The antenna has a low RCS reduction of 41.4dB, but the maximum RCS reduction and gain are lower than our proposed work.

This study proposed a wideband, high gain polarization conversion metamaterials (PCM) to reduce the RCS of the proposed MIMO antenna. The RCS results were reported for incident angles of ($\theta = 0^0$, $\varphi = 0^0$), ($\theta = 60^0$, $\varphi = 0^0$), ($\theta = 75^0$, $\varphi = 0^0$), ($\theta = 60^0$, $\varphi = 45^0$), and ($\theta = 60^0$, $\varphi = 90^0$). The MIMO antenna did not suffer a gain loss. Metamaterials are used as ground planes for MIMO antennas to reduce RCS. Its RCS reduction was reported for angles of ($\theta = 0^0$, $\varphi = 0^0$), ($\theta = 60^0$, $\varphi = 0^0$), ($\theta = 60^0$, $\varphi = 45^0$) and ($\theta = 60^0$, $\varphi = 90^0$). In the rest of the letter, four sections are presented. Section 2 explores the MIMO antenna design process, the suggested antenna geometry, the unit cell metamaterial geometry, and the equivalent circuit model (ECM). Section 3 discusses the integration of the MIMO antenna with PCM and the RCS analysis of the antenna with and without PCM. Section 4 covers the measured results, the hardware prototype, and the diversity analysis.

2. MIMO Antenna Design Methodology

2.1 MIMO Antenna Configuration

The proposed MIMO system geometry is presented in Figure 1. The "W" is used to excite the MIMO antenna, which has the benefit of having a wideband and high gain characteristics. A common ground plane is used so that the signals should have a common reference plane [21]. CST Microwave Studio Suite 2022 is used for MIMO antenna simulation. This antenna is mounted on a dielectric substrate, Roger R03003, with a loss tangent of 0.001 and a relative permittivity of 3. It also has a thickness of 1.5mm. The patches' tips have been cut off to enhance the antenna's impedance width and gain, as depicted in Figure 1. The optimized dimensions are in Table 1, with all measurements in millimeters.

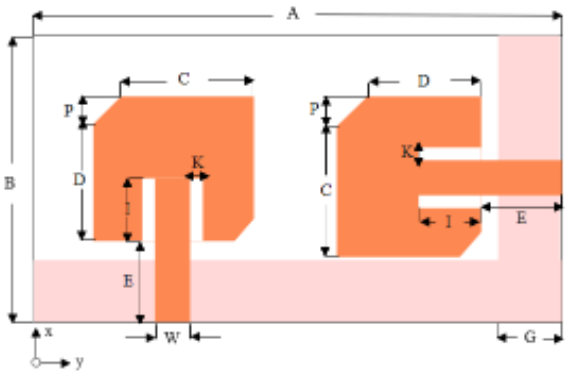

Figure 1: MIMO antenna geometry

Table 1. Dimensions of the proposed RCS antenna

Variables	Size (mm)	Variables	Size (mm)
A	50	H	1.5
B	50	I	3
C	17	K	0.5
D	18.5	M_T	0.035
E	17	P	3.5
G	16.3	W	2.4

2.2 Evolution steps

According to Figure 2, the complete development of the MIMO antenna is illustrated in stages, and In Figure 3, you can observe the simulated S11 results for all the stages. The antenna's bandwidth and gain have been improved through some adjustments made to the patch, specifically by trimming the patch edges. This modification results in a smoother impedance transition and enhances the antenna's bandwidth and gain. The second and third steps involving antennae II and III have successfully achieved impedance matching and improved bandwidth. Antenna III has shown even better performance than antennae I and II. In step 3, the bandwidth extended from 3.1 to 5.6GHz, and there was an increase in bandwidth from 2.8 to 6GHz. A higher frequency band suitable for WLAN at 5.8GHz has also been introduced. Figure 4 depicted the isolation of step 2 and step 3, which is less than -20dB. Figure 5 shows that in Step 1, 3.6dBi of peak realized gain was achieved, 4.8dBi in Step 2, and 5.6dBi in Step 3.

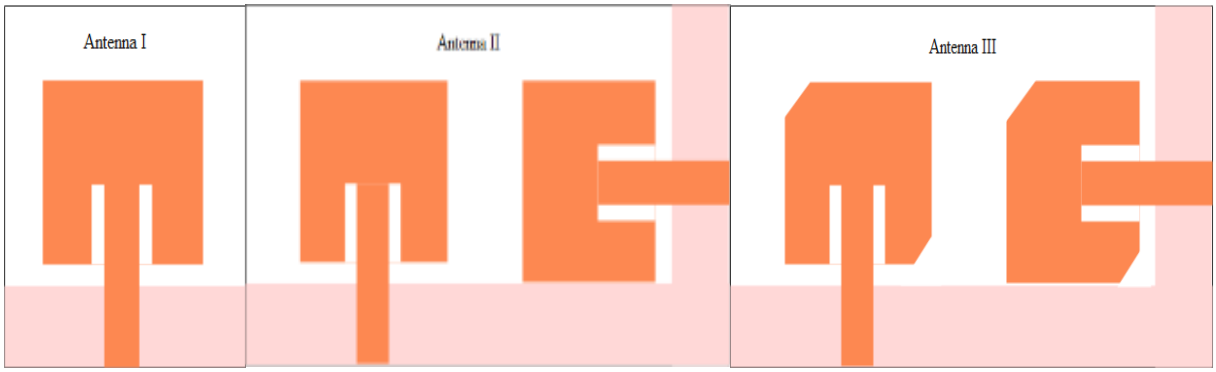

(a) (b) (c)

Figure 2: Evolution steps of the proposed MIMO antenna

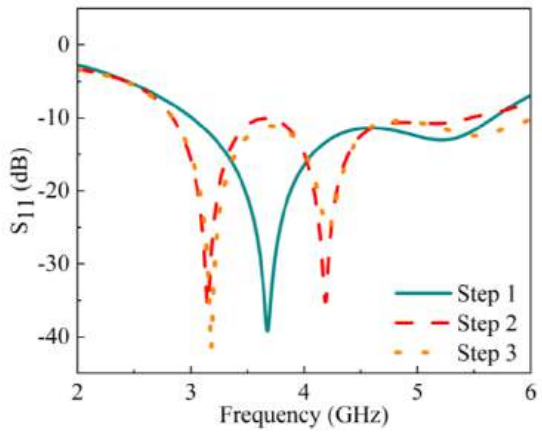

Figure 3: S_{11} of the various stages

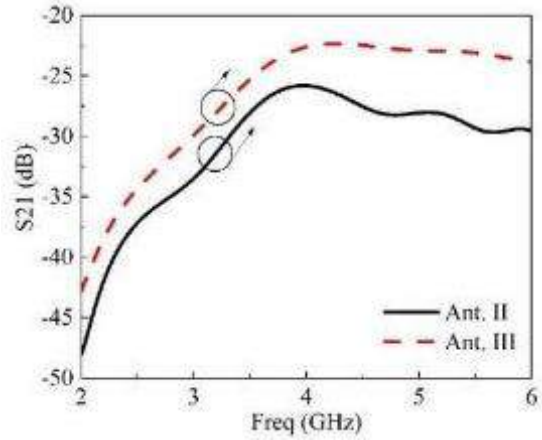

Figure 4: S_{21} of various stages

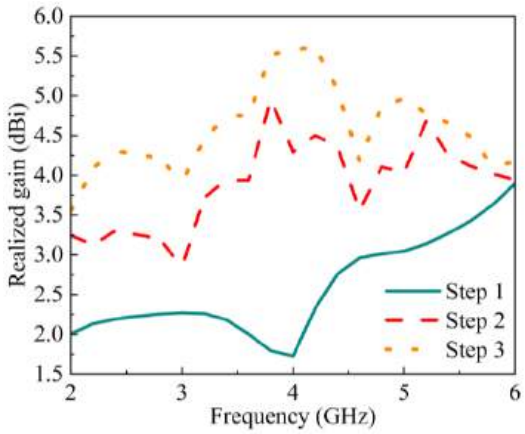

Figure 5: Realized gain of the various stages.

2.3 PCM Design

A polarization conversion metamaterial (PCM) that is applied to a substrate with a relative dielectric constant of 2.2 and a loss tangent of 0.001 is shown in Figure 6. A 1.5mm thick substrate is used. CST Microwave Studio 2022 is adopted to simulate the PCM based on Floquet mode theory [22, 23]. The parameters after optimization are listed in Table 2.

Table 2. PCM design parameters

Parameter	Size (mm)	Parameter	Size (mm)
N	7	L	5
M	7	S	3
R	5	G_1	0.35
V	0.4	G_2	0.35

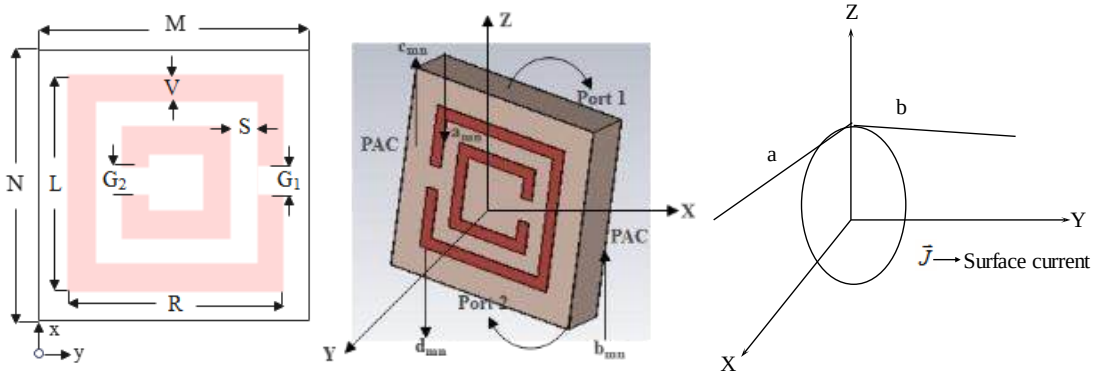

(a) (b) (c)

Figure 6: PCM geometry (a), PCM decomposition (b), Decomposition of surface current (c).

As depicted in Figure 6c, the mathematical definition of $\vec{J}$ is represented by the following equation 1:

$$\vec{J} = f(x, y) \quad (1)$$

Hence, it is possible to express the surface current's x components as shown in equation 2 [24].

$$\vec{J}_x(x, y) = \sum_{m=-\infty}^{\infty} \sum_{n=-\infty}^{\infty} f(x - m_a, y - n_b) \quad (2)$$

In terms of mathematical notation, you can express equation 2 in phase radians as follows, where "m" represents the quantity of unit PMC along the x-axis, "a" denotes the dimension, "n" signifies the amount of unit PMC along the y-axis, and "b" represents the dimension.

$$\vec{J}_x(x, y) = \sum_{m=-\infty}^{\infty} \sum_{n=-\infty}^{\infty} f(x - m_a, yn_b)\, e^{(-jk_{x0}m_a - jk_{y0}n_b} \quad (3)$$

The phase radians along the X and Y-axes, denoted as K_{x0} and K_{y0} can be defined using the equation provided in equations 4 and 5.

$$K_{x0} = k_0 sin\theta_0 cos\theta_0 \quad (4)$$

$$K_{y0} = k_0 sin\theta_0 sin\theta_0 \quad (5)$$

The PCM unit cell will produce a beam directed toward (θ_0, φ_0), while considering the phase angles within the infinite array. By subjecting the surface current, as described in equation (3), to a Fourier transform, we derive the subsequent equation as

$$\vec{J}_x(x,y) = \frac{4\pi^2}{ab}\vec{f}(k_x,k_y)\sum_{m=-\infty}^{\infty}\sum_{n=-\infty}^{\infty}\delta(k_x - k_{xmn})\delta(k_y - k_{ym}) \quad (6)$$

$$K_{xmn} = k_{x0} + \frac{2m\pi}{a} \quad (7)$$

$$K_{ymn} = k_{y0} + \frac{2n\pi}{b} \quad (8)$$

The phase angles, k_x and k_y, are those along the x and y axes. Accordingly, k_{ymn} and k_{xmn} represent the phase angles between ports 1 and 2. Additionally, the unit cell's dimensions are indicated by "a" and "b. The time domain equivalent of equation 6 is as follows.

$$\vec{J}_x(x,y) = \frac{4\pi^2}{ab}\vec{f}(x_y k_y)\sum_{m=-\infty}^{\infty}\sum_{n=-\infty}^{\infty} e^{-(-jk_{xmn}x - jk_{yny})} \quad (9)$$

Fourier transforms in the time domain are represented by $\vec{J}_x(x,y)$ in Figure 6b. The dimensions of the unit cell, denoted as "a" and "b," represent the extent from port 1 to port 2. Floquet mode has been implemented in this configuration to calculate the general scattering matrix. Figure 7a provides a visual representation of the scattering parameter for the PCM unit cell, while Figure 7b displays the real and imaginary permeability curves.

$$\begin{bmatrix} C_{mn}^{TE} \\ C_{mn}^{TM} \\ d_{mn}^{TE} \\ d_{mn}^{TM} \end{bmatrix} = \begin{bmatrix} GSM \\ GSM \\ GSM \\ GSM \end{bmatrix} \begin{bmatrix} a_{mn}^{TE} \\ a_{mn}^{TM} \\ b_{mn}^{TE} \\ b_{mn}^{TM} \end{bmatrix} \quad (10)$$

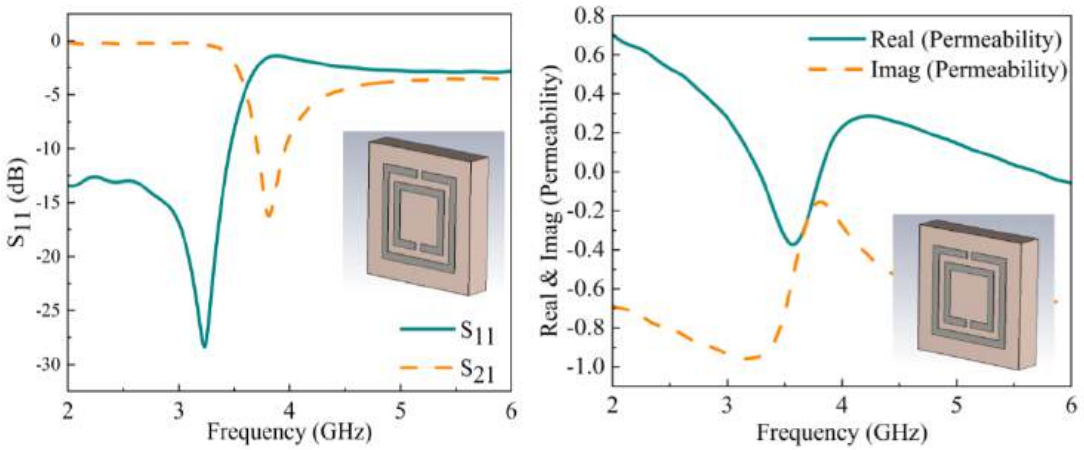

(a) (b)

Figure 7: (a) Scattering parameter for PCM and (b) Real and imaginary permeability for PCM.

2.4 ECM of the Proposed Antenna

Advanced Design System (ADS) software optimized the MIMO antenna's equivalent circuit. Each radiating element can be depicted as a parallel combination of RLC circuits, and these can be derived from the equation provided in Fauri *et al.* [25]. The feeding line is represented by an inductor connected in series with the first parallel RLC circuits on Figure 7. Simultaneously, on the right-hand side, a second inductor is integrated in series with the second set of cascaded RLC circuits to describe the second excitation port. The objective was to optimize the design to cover a frequency range from 1 to 6GHz. A wideband characteristic has been produced after the two cascaded circuits, as shown in Figure 8. The circuit components that have been optimized are listed in Table 3.

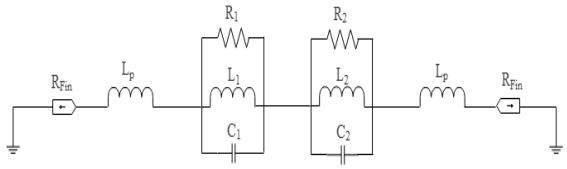

Figure 8: Circuit model for the proposed MIMO antenna

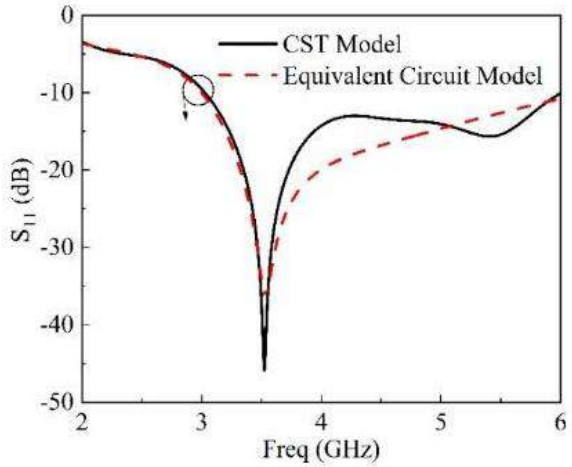

Figure 9: CST model S_{11} and ADS model S_{11}

Table 3. Components used in the circuit optimization

Component	Value	Component	Value
C_1	4.57Pf	L_P	726.5Ph
C_2	818.7Pf	R_1	48.4Ω
L_1	601.7Ph	R_2	34.5Ω
L_2	1.73Ph	R_{FIN}	50Ω

2.5 RCS Reduction

PCM unit cells are used instead of solid metal ground planes for reducing the monostatic RCS of the reference antenna. This advanced ground plane is designed in a specific arrangement, as depicted in Figure 10 PCM unit cells allow electromagnetic waves to reflect within the desired frequency range while passing through out-of-band incident plane waves. By doing so, the antenna's out-of-band monostatic RCS can be effectively reduced without affecting its performance within the desired frequency range. This innovative approach allows for a more efficient reduction of the monostatic RCS while maintaining the antenna.

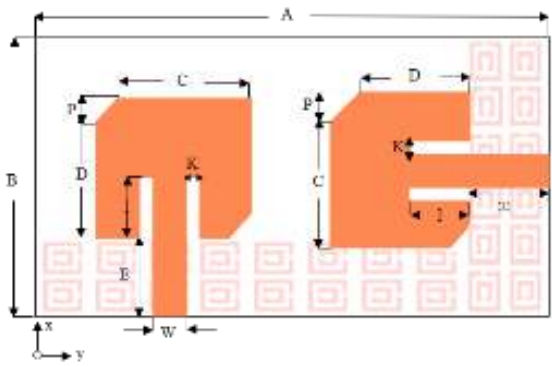

Figure 10: The RCS reduced geometry.

3. Results and Discussion

Radar Cross-sections of the reference and low RCS antennas can be observed in Figure 11 By utilizing a θ-polarized incident plane wave with an amplitude of 1 volt per meter, we were able to attain the subsequent results. Our analysis focused on the incident angles of ($\theta = 0^0$, $\varphi = 0^0$), ($\theta = 60^0$, $\varphi = 0^0$), ($\theta = 75^0$, $\varphi = 0^0$), ($\theta = 60^0$, $\varphi = 45^0$), and ($\theta = 60^0$, $\varphi = 90^0$). Figure 11a reveals that, at 2.8GHz, there's a 5dB reduction in monostatic RCS for normal incidence. The most significant reduction, a remarkable 36dB decrease, occurs at 2.2GHz, and this notable reduction holds across the observed frequency range. For ($\theta = 60^0$, $\varphi = 0^0$) and ($\theta = 75^0$, $\varphi = 0^0$) shown in Figure 11b and 11c, obvious RCS reduction is realized at frequency from 2.8 – 6GHz. The maximum reduction is 48dB at 2.6GHz for ($\theta = 60^0$, $\varphi = 0^0$) and 45dB at the same 2.6GHz for ($\theta = 75^0$, $\varphi = 0^0$). Figures 8d and 8e illustrate a noticeable decrease in RCS within the frequency range of 2.8 to 6GHz when the incident angles are set to ($\theta = 60^0$, $\varphi = 45^0$), and ($\theta = 60^0$, $\varphi = 90^0$).

The radar cross-section decreases when the reference antenna experiences incidents of both normal and oblique co-polarization. Additionally, it is crucial to examine the RCS of the antenna when it is subjected to plane waves polarized at φ. Figure 12 provides a comparison of the RCS for both antennas under φ-polarized incidence, revealing a significant reduction in RCS at incident angles ($\theta = 0^0$, $\varphi = 0^0$) and ($\theta = 15^0$, $\varphi = 0^0$). Figure 13 shows the measured and simulated scattering parameters of the two antennas. It is evident through the measurements that there is a shift at the lowest point of S_{11} due to the fabrication tolerance. The measured and simulated isolation value is more significant than -20 dB.

A prototype for the two-element MIMO antenna was constructed to validate the concept, resulting in a significant reduction in its radar cross-section (RCS). Figures 13a and 13b display the aerial perspectives of the reference antenna from both top and bottom views, whereas Figure 13c showcases the MIMO antenna with a low RCS. Based on Figure 14, it can be observed that the MIMO antenna mentioned in the reference achieves a maximum gain of 5.4dBi at a frequency of 4GHz. Conversely, the low-RCS antenna exhibits a slightly higher gain of 5.6dBi at the same frequency. Consequently, there is a gain increase of 0.2dB for the low RCS antenna in comparison to the reference antenna. The experimental setup for far-field pattern is depicted in Figure 15, and the far-field patterns of both antennas at 3.5GHz, 5.5GHz, and 5.8GHz are displayed in Figures 16, 17, and 18. The strong agreement between the results obtained from simulations and measurements confirms the credibility and validity of the conducted validation.

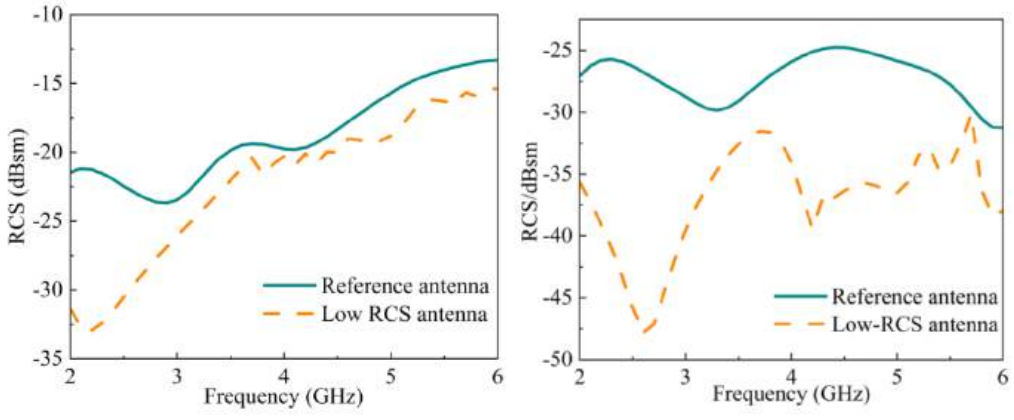

(a) (b)

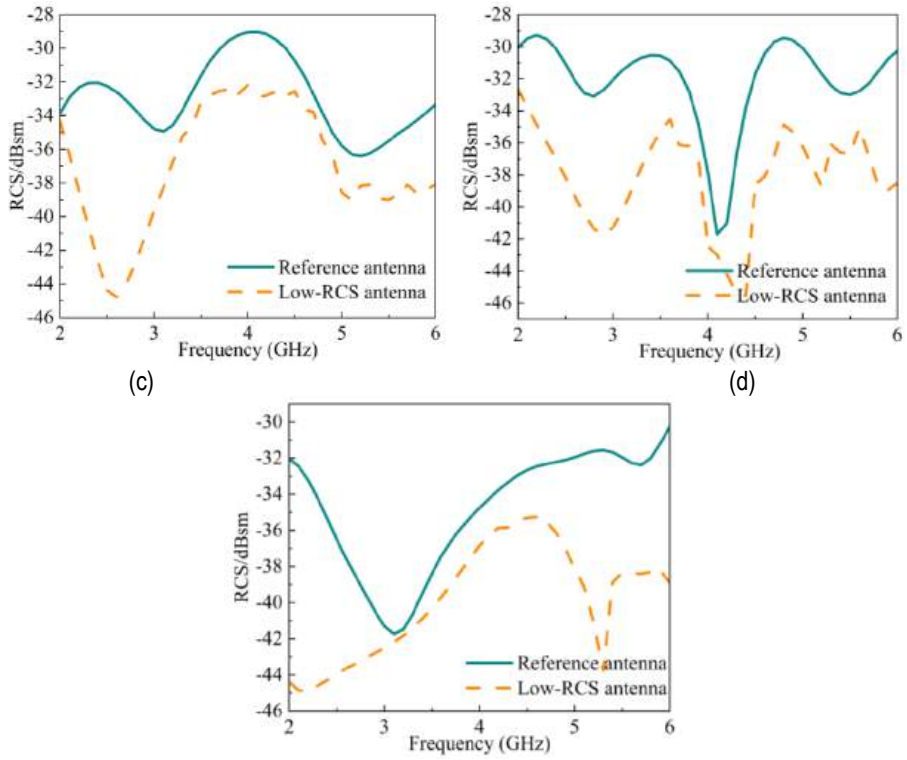

Figure 11: The radar cross-section (RCS) of the reference antenna and low RCS antenna under θ-polarized incidence (a) (θ = 0^0, φ = 0^0), (b) (θ = 60^0, φ = 0^0), (c) (θ = 75^0, φ = 0^0), (d) (θ = 60^0, φ = 45^0), (e) (θ = 60^0, φ = 90^0).

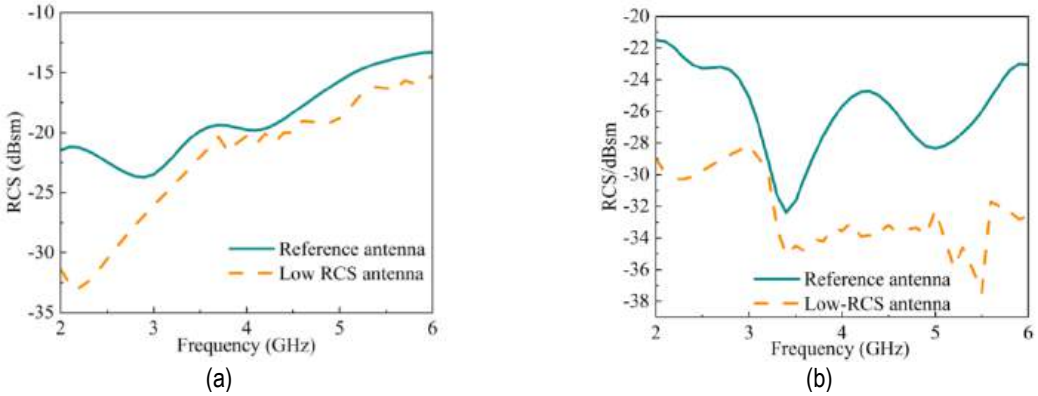

Figure 12: The radar cross-section (RCS) of the reference antenna and low RCS antenna under φ-polarized incidence (a) (θ = 0^0, φ = 0^0), (b) (θ = 15^0, φ = 0^0).

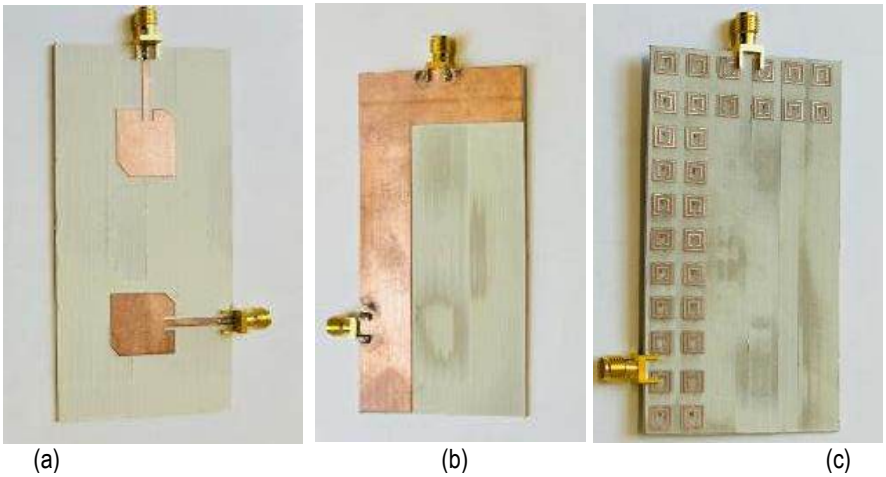

Figure 13: Fabricated prototype (a) Front view, (b) Back view, (c) Low-RCS antenna

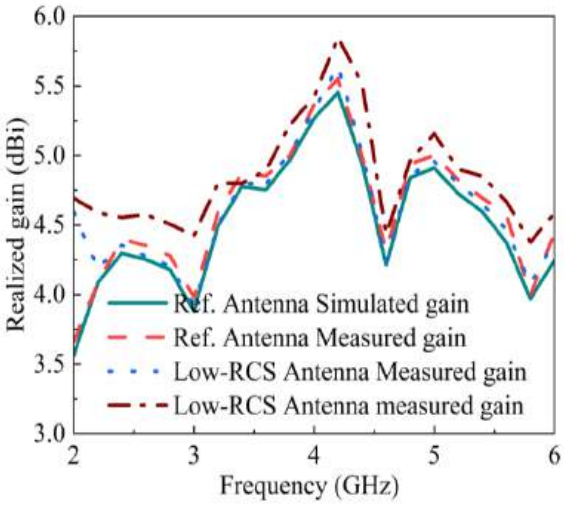

Figure 14: Gain insight into reference and low RCS antenna.

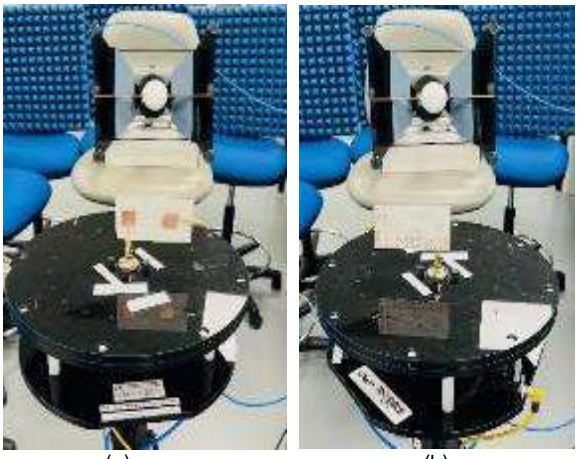

(a) (b)

Figure 15: Far-field experimental setup for (a) reference antenna, (b) low-RCS antenna

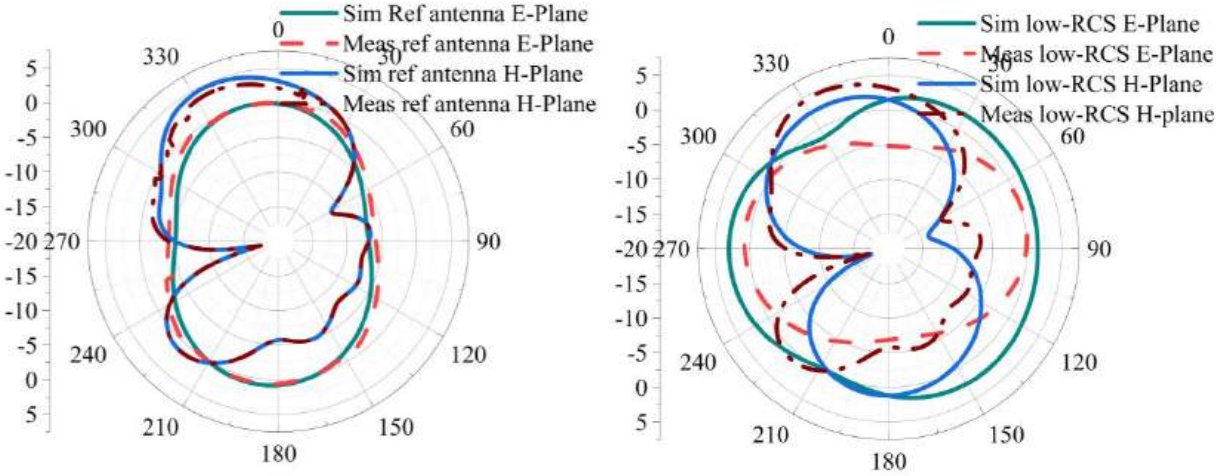

(a) (b)

Figure 16: Far-field pattern at 3.5GHz, (a) reference antenna, (b) low-RCS antenna

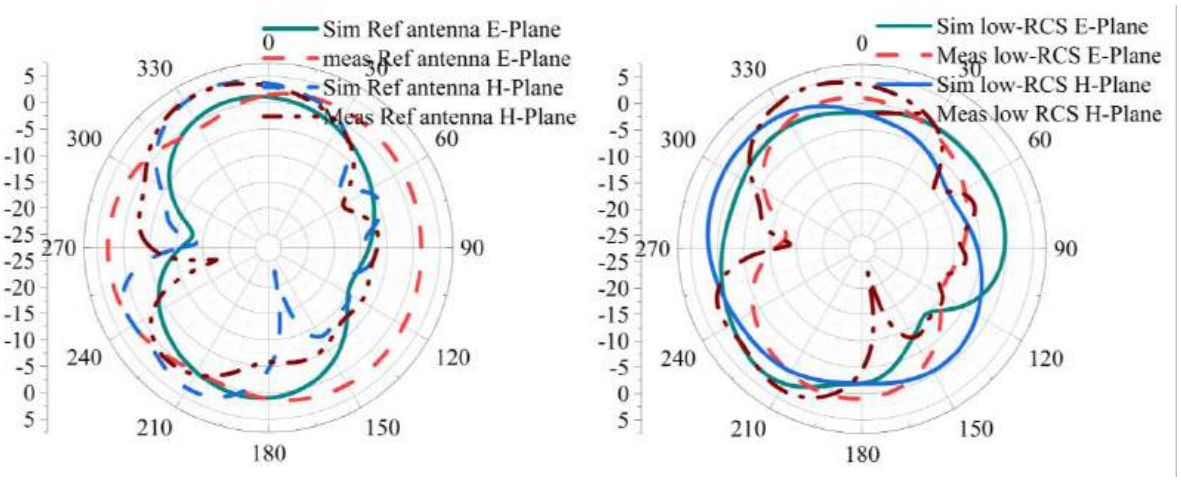

(a) (b)

Figure 17: Far-field pattern at 5.5GHz, (a) reference antenna, (b) low-RCS antenna

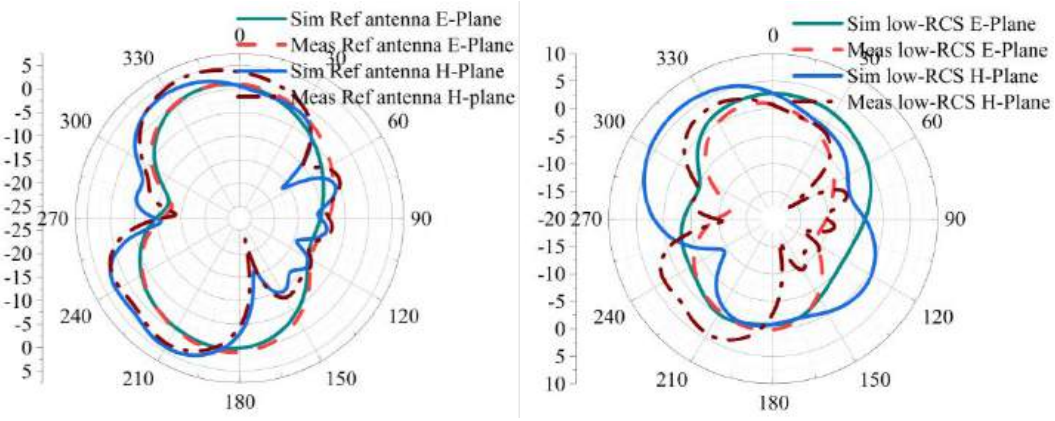

(a) (b)

Figure 18: Far-field pattern at 5.8GHz, (a) reference antenna, (b) low-RCS antenna

The surface current distribution of the reference and low-RCS antenna at various frequencies was mapped using the CST simulator. Consequently, Figures 19 and 20 display the surface current distribution on the rectangular patch-loaded radiators at specific frequencies, with red indicating the highest current distribution areas and blue signifying the lowest.

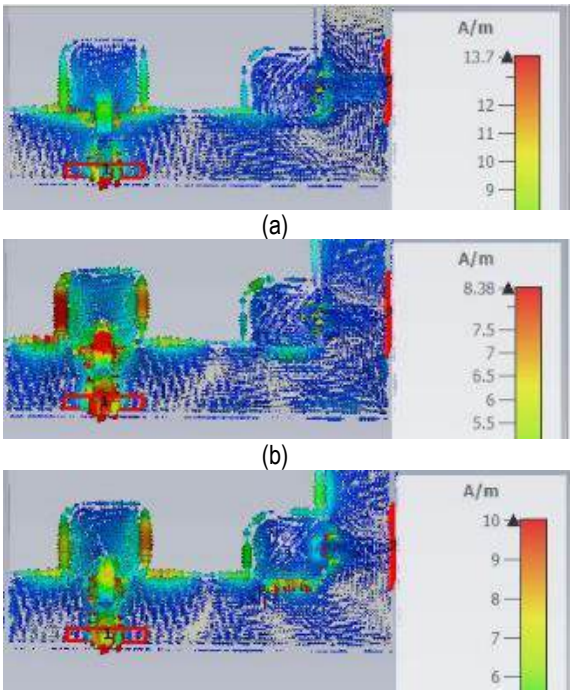

(a)

(b)

(c)

Figure 19: Surface current distribution for reference antenna at (a) 3.5GHz, (b) 5.5GHz, (c) 5.8GHz

4. MIMO Performance measurement

A comprehensive analysis is conducted on the MIMO antenna to assess its diversity performance characteristics. This analysis encompasses various factors such as the Total Active Reflection Coefficient, Channel Capacity Loss, Diversity gain, Envelope Correlation Coefficient, and Mean Effective Gain. The aim is to thoroughly evaluate the antenna's performance in terms of diversity and its impact on signal quality and transmission efficiency.

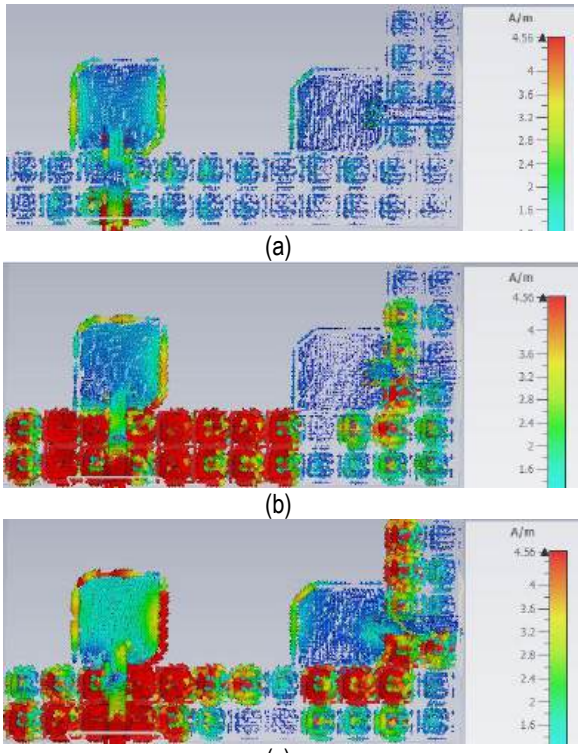

(a)

(b)

(c)

Figure 20: Surface current distribution for low-RCS antenna at (a) 3.5GHz, (b) 5.5GHz, (c) 5.8GHz.

ECC represents the level of isolation between two antennas, and it is considered acceptable when it is zero. However, in practical scenarios, ECC values below 0.5 are also deemed acceptable. The ECC can be determined using either the S-parameter or far-field techniques, as shown in Figure 21. The calculated ECC for the proposed antenna falls below the practical limit within the frequency range of 2.8 – 6GHz. TARC, on the other hand, is a metric used to assess the isolation between antenna elements. It is calculated by comparing the total reflected power to the incident power. Figure 22 illustrates the TARC values obtained from both simulated and measured data, ranging from 00 to 600 intervals. It is evident that the TARC remains below -10 dB throughout. Diversity gain refers to the amount of power transmitted without any performance loss when incorporating diversity schemes. It also enhances the signal-

to-interference ratio. Figure 23 demonstrates that the DG value for both the reference and low-RCS antennas exceeds 10dB. Moving on to the MEG, it measures the antenna's capability to receive electromagnetic waves. In Figure 24, the MEG remains below -3dB for both the reference and low-RCS antennas. Lastly, the transmission loss is evaluated using CCL, which should ideally be below 0.4 bits/s/Hz. Figure 25 showcases the measured and simulated CCL values for both types of antennas, satisfying practical expectations. The bandwidth dimensional ratio (BDR) is computed to measure the antenna's compression, as described in [30].

Table 4. Comparison of reported RCS antennas

References	Size		Isolation (dB)	Max. Gain (dB)	Max. RCS Reduction (dB)	BDR
	mm^2	$\lambda_0 \times \lambda_0$				
[7]	48x148	0.7x0.7	15	4.0	20	47
[9]	50x99	0.63x1.24	13	6.3	18	1.67
[10]	55x45	1.62x1.32	20	4.8	24	1.31
[11]	33x17.8	0.33x0.18	17.5	3.5	20	2500
[12]	50x100	1.25x2.5	46	4.8	7	19.2
[15]	54x54	1.44x1.44	-	5.9	29	26.3
[16]	192x192	5.6x5.6	-	-	20	0.18
[19]	84x84	1.65x1.65	-	2.1	28	1.87
This work	50x50	0.47x0.47	22	5.6	48	226.3

$$BDR = \frac{\%BW}{\lambda_w \times \lambda_L} \quad (10)$$

Given that the proposed antenna combines wideband capability with low-RCS characteristics, it is evaluated against several antennas documented in Table 4. In comparison to the majority of antennas reported in the literature, the presented antenna demonstrates minimal mutual coupling, realized gain, and the most substantial reduction in RCS

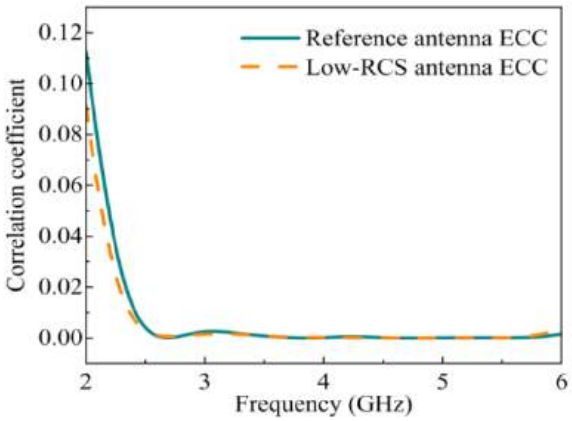

Figure 21: Reference and low-RCS antenna's ECC

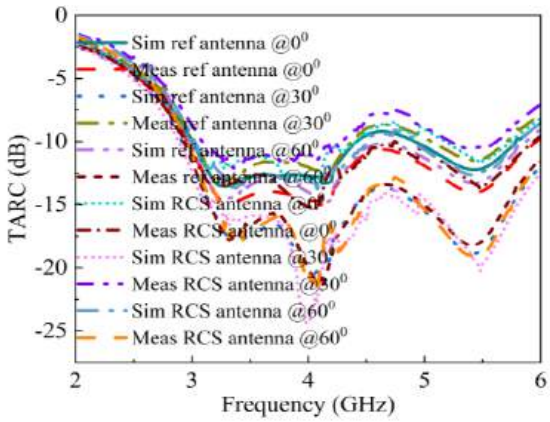

Figure 22: Measured and simulated TARC for reference and low-RCS antenna.

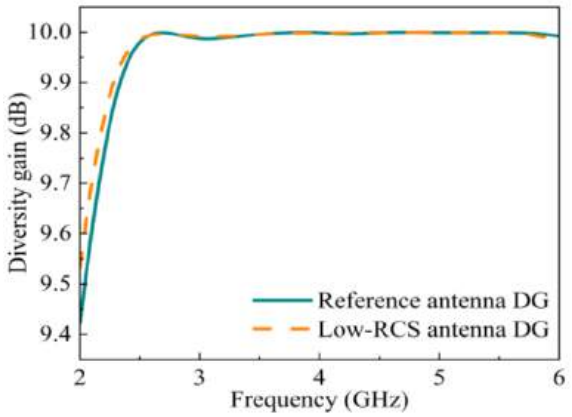

Figure 23: DG for reference and low-RCS antenna

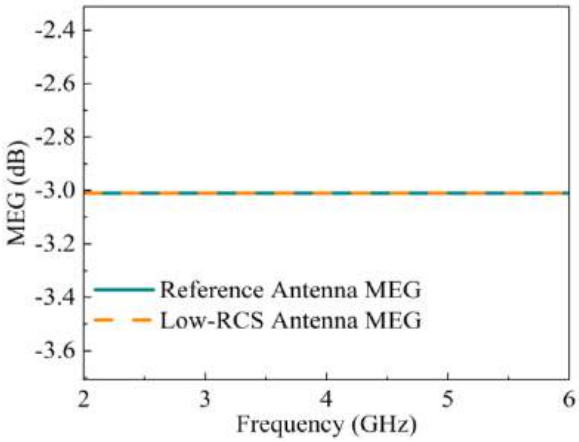

Figure 24: MEG for reference and low-RCS antenna

5. Conclusion

This paper presents a PMC-based wideband MIMO antenna with low RCS and high gain. The primary objective of the design is to create a MIMO antenna that offers low RCS and high gain while covering a broad frequency range from 2 to 6GHz. The paper also presents an equivalent circuit model for the antenna, which aligns reasonably well with the results obtained from full-wave simulations.

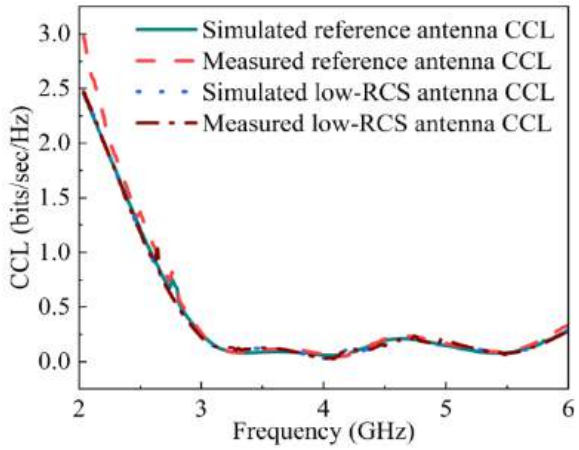

Figure 25: Measured and simulated CCL for reference and low-RCS antenna

The MIMO antenna demonstrates a noticeable reduction in RCS, a wide impedance bandwidth with levels less than -10dB, and isolation exceeding 20dB within the 2.8 to 6GHz range. It also achieves a higher gain of 5.6 dBi around the 4GHz frequency. Furthermore, the antenna exhibits exceptional diversity performance in ECC, TARC, DG, CCL and MEG.

Acknowledgments

The authors thank their affiliated universities and institutes for providing research facilities.

References

[1]. Pattanaik, B. and Chauhan, A., (2023). A study of stealth technology, *Materials Today: Proceeding*, 81(2), 543-546

[2]. Singh, K., Afzal, M. U., Lalbakhsh, A. and Esselle, P. K., (2021). *Reflecting phase gradient metasurface for radar cross section reduction*, 2021 IEEE Asia Pacific Microwave Conference (APMC) Brisbane Australia, pp. 344 – 346.

[3]. Elsewedy, M. F. and Abdallah, M. A., (2023). A monostatic and bistatic RCS reduction using artificial magnetic conductor metasurface, *IEEE Transactions on Antennas and Propagation*, 71(2), 1988 – 1992.

[4]. Huang, X. Zhao, Z. and Wan. G., (2020). *A slotted frequency selective surface with its application in microstrip antenna RCS reduction*, 2020 IEEE 3rd International Conference on Electronics Technology (ICET), Chengdu, China, pp. 724 – 728.

[5]. Jian, Q., Duan, J., Uddin, A., Wu, X., Yi, H. and Wu L., (2023). A waffle structured composite for RCS reduction via absorption and scattering mechanisms, *Materials and Design*, 226, 1-11.

[6]. San, H., Jia, Y., Liu, Y. and Wang, X., (2021). *In-band RCS reduction of a microstrip array antenna based on phase control metasurface*, 2021 International Conference on Microwave and Millimeter Wave Technology (ICMMT), Nanjing, China, pp. 1-2.

[7]. Thummaluru, S, R., Kumar, R. and Chaudhary, R. K., (2015). Isolation enhancement and radar cross section reduction of MIMO antenna with frequency selective surface, *IEEE Transaction on Antennas and Propagation*, 66, 1595 – 1600.

[8]. Lu, J., Zhang, H. C., Shao, C., Wei, C. and Cui, T. J., (2022). Design of compact multiple-input-multiple-output antenna based on slow waves corrugated strips, *IET Microwave Antennas Propagation*, 16(9), 617 – 626.

[9]. Das, P., Saha, C. and Mandal, K., (2022). *Mutual coupling and RCS reduction of MIMO antenna using a hybrid technique*, 2022 IEEE Wireless Antennas and Microwave Symposium (WAMS), 2022, pp. 1 - 5.

[10]. Saxena, G., Awasthi, Y. K. and Jain, P., (2021). Design of metasurface absorber for low RCS and high isolation MIMO antenna for radio location and navigation, *International Journal of Electronics and Communication*, 133, 1- 10.

[11]. Khoiramizadeh, M. and Ali-Nezhad, S. M., (2021). Radar cross section reduction of a UWB MIMO antenna using image theory and its equivalent circuit model, *International Journal of RF Microwave Computer-Aided Engineering*, 31(3) 2256 - 2263.

[12]. Das, P. and Mandal, K., (2022). Polarization conversion surface integrated MIMO antenna for simultaneous reduction of RCS and mutual coupling, *IEEE Antennas and Wireless Propagation Letters*, 21(9), 1782 – 1786.

[13]. Gao, X., Yin, S., Wang, G., Xue C. and Xie, X., (2022). Broadband low-RCS circularly polarized antenna realized by non-uniform metasurface, *IEEE Antennas and Wireless Propagation Letters*, 21(12), 2417 – 2421.

[14]. Soliman, S. A. M., EL-desouki, E. M, EL-nady, S. M. and Abd El-Hameed A. S., (2023). Broadband low RCS based pn polarization dependent artificial magnetic conductor metasurface, *IEEE Access*, 11, 53176 – 53184.

[15]. Wang P., Jia Y., Liu Y. and Hu, W., (2022). A wideband low-RCS circularly polarized reconfigurable C-shaped antenna array based on liquid metal, *IEEE Transaction on Antennas and Propagation*, 70(9), 8020 – 8029.

[16]. Li J., Ali Khan T., Meng X., Chen J., Peng G. and Zhang, A., (2019). Wideband radar cross section reduction of microstrip patch antenna using coding metasurface, *IET Microwave Antenna and Propagation*, 13(10), 1719 -1725.

[17]. Zhang, Z., Liu T., Cao X., Yang H., Jidi L. and Gao, J., (2022). An integrated 2-bit metasurface array antenna with broadband low radar cross section covering large incident angle space, *IET Microwave Antennas Propagation*, 16(6), 369 – 377.

[18]. Deng, S., Zhang, X., Dung, J., Zhang H., Chen W., Zhang Z. and Chen, C., (2023). Low profile high gain broadband circularly polarized slot antenna with RCS reduction using polarization conversion metasurface, *Microwave Optical Technological Letters*, 65, 281 -289.

[19]. Jiang, H., Xue, Z., Zenq, Q., Li, W. and Ren, W., (2018). High gain low RCS antenna array based on

checkerboard surface, *IET Microwave Antennas Propagation*, 12(2), 237 – 240.

[20]. Deepti, I., Gangwar, D., Singh, S., Sharma, A., Singh, S. P. and Lay-Ekuakille, A., (2022). Design of polarization conversion metasurface for RCS reduction and gain improvement of patch antenna for Ku band radar sensing applications, *Sensors and Actuators*, 333, 1 – 12.

[21]. Sharawi, M. S., (2017). Current misuses and future prospects for printed multiple-input-multiple-output antenna systems, *IEEE Antennas and Wireless Propagation Magazines*, 59(2), 162 – 170

[22]. Fantoni, F., Morini, L., Bacigalupo, A. and Paggi M., (2021). The generalized floquet block spectrum for periodic thermos-diffusive layered materials, *International Journal of Mechanical Sciences*, 194, 106178.

[23]. Chen, Q., Mesa, F., Lin, X., Yin X. and Quevedo-Teruel, O., (2020). Accurate characterization and design guidelines of glide symmetric holey EBG, *IEEE Transaction on Microwave Theory and Technique*, 68(12), 4984-4994.

[24]. Rohan, E., Nguyen, V. H. and Naili, S., (2021). Homogenization approach and floquet bloch spectrum for wave analysis in fluid saturated porous media with mesoscopic heterogeneities, *Applied Mathematical Modelling*, 91, 1-23.

[25]. Fauri, Y., Ahmad, S., Naseer, S., Alhammami, K., Awad, N., Ghaffar, A. and Hussein, M. I., (2022). Compact super-wideband frequency diversity hexagonal shaped monopole antenna with switchable rejection band, *IEEE Access*, 10, 42321-42333.

[26]. Ibrahim, A. A., Ahmed, M. I. and Ahmed, M. F., (2021). A systematic investigation of four port MIMO antenna depending on flexible material for UWB networks, *Scientific Reports*, 12, 2608

[27]. Kumar, A. A., Abdul, Q., Kanaujia, B. K. and Kishor, J. I., (2019). A novel ITI-shaped isolation structure placed between two port CPW-fed dual-band MIMO antenna for high isolation, *International Journal of Electronics and Communication*, 104(1) 35 – 43..

[28]. Jabire, A. H., Sani, S., Saminu, S., Adamu M. J. and Hussein, M. I., (2023). A crossed polarized four port MIMO antenna for UWB communication, *Heliyon*, 9, 1-14.

[29]. Baz, A., Jansari, D., Lavadiya, S. P. and Patel S. K., (2023). Miniaturized and high gain circularly slotted 4x4 MIMO antenna with diversity performance analysis for 5G/WiFi/WLAN wireless communication applications, *Results In Engineering*, 20, 1 – 12.

[30]. Lodhi, D. and Singhal, S., (2023). CPW fed shovel shaped super wideband MIMO antenna for 5G applications', *International Journal of Electronics and Communication*, 168, 1 – 14.